

Porous Carbon Nanofibers Supported Zn@MnOx Sorbents with High Dispersion and Loading for Hot Coal Gas Desulfurization

Yuekun Lai¹, Yu Feng², Man Zhang², Yangjie Sun³, Caimei Long², Jiancheng Wang², Xiurong Ren², Mingzheng Ge², Chunyan Cao², Weilong Cai², and Jie Mi²

¹Fuzhou University

²Affiliation not available

³Taiyuan University of Technology

September 21, 2022

Abstract

Sorbent with a great quantity of highly dispersed active components is of importance to achieve excellent desulfurization performance. Thus, Zn@MnOx/porous carbon nanofibers (PCNFs) sorbents have been constructed via electrospinning, carbonization, activation and hydrothermal techniques in this study. The as-prepared sorbent realizes a sulfur capacity of 9.63 g S 100 g⁻¹ sorbent and a utilization rate 117% of ZnO, which could be attributed to the synergetic effects of the enlarged surface area of PCNFs and uniformly distributed active components. The specific surface area of modified PCNFs is nearly five times higher than that of the pristine CNFs, providing larger loading area and more attachment sites for metal oxides. Activation with KMnO₄ not only generates active MnOx components but also presets ‘seed’ for ZnO crystals growth, which is beneficial for the high dispersion of nano-sized active components. The presented method is beneficial to producing sorbents with better structure and promoted desulfurization performance.

1. Introduction

Coal consumption has been increased from 2830 million tons to 2934 million tons in China in 2021.¹ The clean and efficient utilization of coal thus becomes significant for the country to achieve the strategic goal of “Emission peak and carbon neutralization”. Nevertheless, in the clean transformation of coal, coal gas, as an indispensable raw material and power source, corrodes equipment and causes catalyst poisoning in subsequent processes, for the presence of H₂S in it.² Therefore, removal of H₂S is an important prerequisite for the clean utilization of coal.³

Among the existed techniques of H₂S removal, dry desulfurization, compared with wet desulfurization, is widely employed in the situations at medium and high temperatures, which not only makes full use of the sensible heat of coal gas, but also reduces the consumption for raw coal in coal-fired system.⁴ High temperature coal gas desulfurization is realized through the reaction between single or composited metal oxides and H₂S with metal sulfide as products. Theoretically, the more active components the better sulfur capacity of desulfurization sorbent.^{5,6} However, previous studies reveal that the pure metal oxides own a poor sulfur capacity due to the aggregated oxide grains and undesirable plugged structures, resulting in insufficient utilization of active components.^{7,8} In order to solve this problem, porous supporters such as activated carbon, zeolites, γ -Al₂O₃ and molecular sieve have been introduced into the preparation of sorbent.⁹⁻¹¹ Liu et al. synthesized desulfurization sorbent with highly dispersion of active components by combining porous MAS-9 and Ca-based oxides.¹² It was found that the sorbent exhibited a sulfur capacity of 17.16 g S 100 g⁻¹ sorbent. Mi et al. applied MCM-41 as porous supporter to promote the desulfurization performance of ZnO-based sorbent.¹³ They achieved a sulfur capacity of 5.7 g S 100 g⁻¹ sorbent due to the uniform distribution of ZnO

nanophase on MCM-41. However, the utilization rate of the ZnO/MCM-41 sorbent is low (57%), which differs greatly from the theoretical value. The key to removing hydrogen sulfide is the replacement process of O^{2-} (radius 0.140 nm) in metal oxide and S^{2-} (radius 0.184 nm) in hydrogen sulfide, but the greater molecular volume of metal sulfide than that of the metal oxide is bound to occupy a larger space.¹⁴ While within the sorbent preparation with porous solid supporters, the active components are expected to scatter in the internal surface of channels, the induced volume expansion of desulfurization products is likely to fill and plug the inner channel of supporters, which happens in the “pore closing” process, finally limiting the mass transfer and ion diffusion of the reaction. Besides, though the rich channels of meso-supporter contribute high surface area, they are also easily to be plugged due to the limited pore size, which cannot meet the requirements for desulfurization applications that need massive reaction agent.

To overcome the above challenges, carbon nanofibers (CNFs) with large specific surface area and opening three-dimensional structure have been proposed into preparing desulfurization sorbent.^{15,16} For example, Bajaj et al. investigated the synergetic effect of activated carbon nanofibers (ACNFs) and Cu_xO nanoparticles for coal gas desulfurization. They found that ACNFs as supporting matrix play an important role in preventing aggregation of nanoparticles.¹⁷ Similar results have also been obtained by Kim et al., where the CNFs-supported sorbent showed 3 times higher in ZnO utilization efficiency compared to pure ZnO nanopowders.¹⁸ However, the loading content and dispersion of active components are heavily influenced by the limited surface area of CNFs. Besides, the preparation strategy applied lowers the utilization of active components due to the fact that metal ions are encapsulated by CNFs. By learning from these strategies and the opening three-dimensional structure of CNFs, we hypothesize that an enlarged surface area for desulfurization sorbent by introducing the CNFs supporter with high specific surface area and porous structural features with ease gas diffusion performance, which are beneficial for the uniform distribution of massive active components and increase its loading content (**Figure. 1a**). More important, CNFs are conducive to the avoidance of the negative effects arising from the volume expansion of the desulfurization products based on its opening structure and flexibility. Upon the hypothesis, the CNFs materials with enlarged surface are expected to provide a much wider supporter area for active components and thus achieve a highly dispersed distribution, which can promote the loading content and utilization of desulfurization sorbent.

In this work, a surface area enlarged structure of $Zn@MnO_x$ /porous CNFs (PCNFs) desulfurization sorbent with highly dispersed active components is rationally constructed by electrospinning, carbonization, etching, oxidation activation and hydrothermal treatments, which facilitates improving the loading content and utilization of active component. PCNFs were obtained by taking SiO_2 as sacrifice phase after the co-electrospinning of polymers and SiO_2 . The PCNFs are effective in increasing specific surface area, which is beneficial for keeping active components distributed in small grain size. Manganese oxides derived from oxidation activation by $KMnO_4$ not only serve as active components for desulfurization, but also as acts as seeds for the growth of ZnO on PCNFs. Benefited from our rational structure design, the desulfurization performances of the as-prepared sorbents tested with a fixed-bed reactor at 500 °C achieves 9.63 g S 100 g⁻¹ sorbent, with an overall utilization rate of active components up to 73%. It is worth noted that the utilization rate of ZnO reached up to 117% at the breakthrough concentration of 900 ppm.

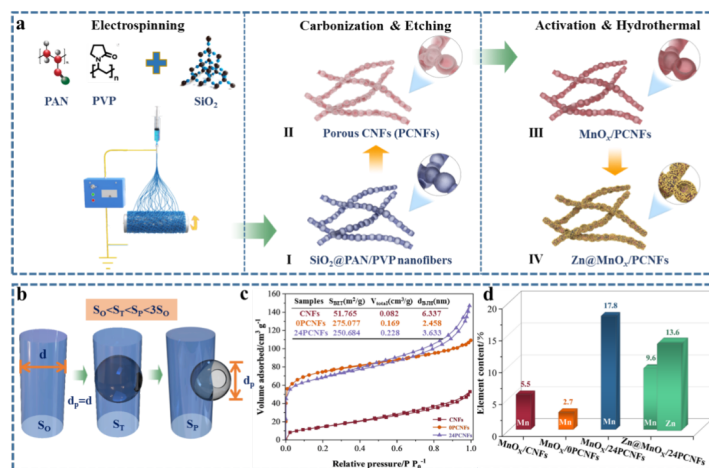


Figure 1 . (a) Schematic illustration of synthesis of ZnY@MnO_x/XPCNFs sorbent. (b) Schematic illustration of the surface areas of CNFs and PCNFs. (c) Structural parameters of pristine CNFs, 0PCNFs and 24PCNFs. (d) Loading contents of Mn in sorbents MnO_x/CNFs, MnO_x/0PCNFs, MnO_x/24PCNFs and Zn@MnO_x/24PCNFs.

First, the surface area enlargement of pristine CNFs and PCNFs is theoretically studied to rationally guide structural tuning of CNFs supporter (Figure. 1a). SiO₂ nanospheres were introduced into the electrospun PAN matrix as hard template for the purpose of expanding the surface area and attachment sites for metal oxides. Herein, as shown in Figure. 1b, assuming the single nanofiber in pristine CNFs is a cylinder with diameter (d) [?] 0.1 mm and height [?] 0.1 mm, the lateral area S₀ of the single nanofiber is 0.1256 mm². In the meantime, the diameter (d_p) of the hollow carbon shell derived from the etching of SiO₂ sphere is assumed equal to d of the cylinder. Based on the above hypothesis, after the introduction and etching of SiO₂, the S_T and S_P of the enlarged single nanofiber calculated are 0.2405 and 0.2856 mm², respectively, which are 1.9 and 2.3 times higher than that of the pristine CNFs. Theoretically, the highest area of enlarged single nanofiber can reach up to 0.3556 mm², more than 2.8 times higher than that of the pristine CNFs (Figure. S1). According to the models established and the calculations, our hypothesis is beneficial for an enlarged and expanded surface area of porous CNFs.

Besides, N₂ adsorption-desorption was applied to analysis the structural parameters of the modified PCNFs (Figure. 1c). The strategy employed successfully enlarges the specific surface area and total pore volume from 51.765 m²g⁻¹ and 0.082 cm³g⁻¹ to 250.684 m²g⁻¹ and 0.228 cm³g⁻¹, which realizes amplifications of 483% and 278%, respectively. Furthermore, the pristine CNFs, PCNFs were processed through activation oxidation in KMnO₄ solution for the adherent of MnO_x. ICP characterization verified the same trend in Mn²⁺ content as structural parameters display. The Mn²⁺ content in sorbent MnO_x/24PCNFs is 17.8%, while it's only 5.5% in sorbent with pristine CNFs as supporter. According to the above results, it can be seen that this unique desulfurization sorbent using the surface area enlarged PCNFs as supporter could provide expanded surface area and a plenty of attachment sites for the loading of active components. Besides, the three dimensional opening structure of the modified CNFs will improve the mass transfer and ion diffusion rate of the corresponding desulfurization sorbent.

2. Results and discussion

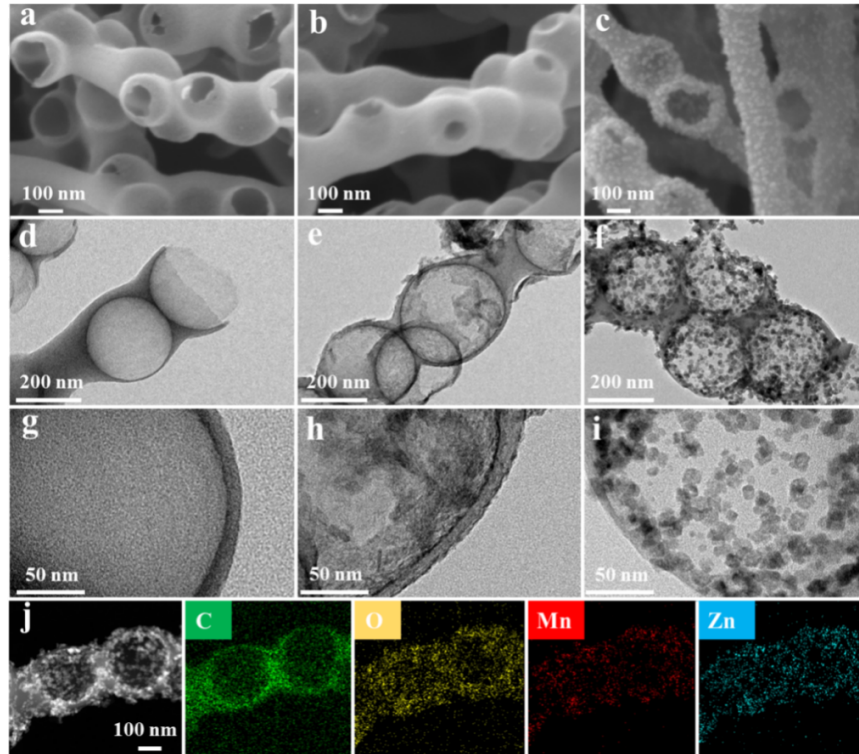


Figure 2 . SEM and TEM graphs of (a, d, g) 24PCNFs, (b, e, h) MnO_x /24PCNFs and (c, f, i) Zn@MnO_x /24PCNFs. (j) EDX graphs of elements C, O, Mn and Zn within sorbent Zn@MnO_x /24PCNFs.

The morphology of the modified CNFs and the supported sorbents after electrospinning, heat treatment and etching was characterized via SEM (**Figures. 2** and S2). As shown in Figure. 2a, 24PCNFs exhibit the characteristics of smooth surface and 3D continuously interconnected networks with hollow carbon shells uniformly embedded. In addition, as displayed in Figure. S2, supporters CNFs, 0PCNFs, 8PCNFs, 16PCNFs and 32PCNFs were also prepared to uncover the effect of the compositions of spinning solution on the morphology of carbon nanofibers. It can be seen that the morphology of CNFs (Figure. S2a) is smooth surface and no significant pore structure have been observed, which is similar to that of 0PCNFs (Figure. S2b). When the content of SiO₂ increased from 0 to 8 wt.%, the content of embedded hollow carbon shells in 8PCNFs was less and still retained most of the morphology of 0PCNFs (Figure. S2c). With the increase of the content of hollow carbon shells embedded on porous carbon nanofibers, the original micro-structure of 0PCNFs was completely changed. However, the content of hollow carbon shells embedded on 16PCNFs was significantly lower than that of 24PCNFs, which show little potential for the purpose of enlarging the surface area of CNFs (Figures. S2d and e). The content of carbon shells embedded on carbon nanofibers is limited when the polymer content in the electrospinning solution is certain. Due to the excessive SiO₂ content, the hollow carbon shells on 32PCNFs were no longer distributed uniformly along the fibers, the aggregation phenomenon increased, and the fiber fracture was aggravated (Figure. S2f). In conclusion, the morphology of 24PCNFs were consistent with the preset expectation of the optimal supporter.

Due to the surface hydrophobicity and chemical inertness, KMnO₄ oxidation was adopted in order to anchor the manganese oxide uniformly on the carbon nanofibers based on the reaction: $\text{MnO}_4^- + \text{C} + \text{H}_2\text{O} - \text{MnO}_2 + \text{CO}_3^{2-} + \text{HCO}_3^-$.¹⁹ As show in Figure. 2b, the morphology of MnO_x /24PCNFs oxidized under 30 °C is similar to that of 24PCNFs, and no obvious observations involved manganese oxide particles have been found upon the supporter 24PCNFs, indicating that the structure of porous carbon nanofibers after the oxidation process is well preserved under 30 °C (Figure. S3a). 24PCNFs were also oxidized at 45 and 60 °C

for increasing the loading of manganese oxides, however, compared with MnO_x /24PCNFs oxidized at 30 °C, fractures and cracks have been observed within the 24PCNFs processed at 45 and 60 °C (Figures. S3b and c). Therefore, 30 °C is selected as the optimal activation temperature of 24PCNFs, which is to maintain the completeness and continuous characteristics of activated MnO_x /24PCNFs sorbent. MnO_x /CNFs and MnO_x /XPCNFs were prepared under the same oxidation parameters to investigate the effect of different structure and morphology of carbon nanofibers on the loading content of manganese oxide anchored on them. As displayed in the SEM images of sorbents MnO_x /CNFs and MnO_x /XPCNFs (Figures. S4a-f), the activated sorbents remained structural integrity, except the sorbent supported by 32PCNFs, which appeared fractures within the nanofibers (Figure. S4f). The loading content of element Mn in the sorbent was tested by ICP. The order of MnO_x /32PCNFs > MnO_x /24PCNFs > MnO_x /16PCNFs > MnO_x /8PCNFs > MnO_x /CNFs > MnO_x /0PCNFs based on the manganese oxide content loaded is proposed (Table S1). The results show that the embedded hollow carbon shells greatly increase the number of anchor sites and improve the loading of the active components. Furthermore, by comparing the integrity of the oxidized CNFs and desulfurization performance of the corresponding sorbents, 24PCNFs was seemed as the optimal supporter and the sorbent MnO_x /24PCNFs was selected as ‘seed’ for further investigation for the bi-oxides desulfurization sorbents.²⁰

As shown in Figure. 2c, namely the SEM graph of sorbent Zn@MnO_x /24PCNFs, nano particles with uniform size and evenly distribution appeared on the surface of porous carbon nanofibers, of which the structure completeness did not change obviously. In addition, sorbents Zn0@MnO_x /24PCNFs, Zn2@MnO_x /24PCNFs and Zn3@MnO_x /24PCNFs were also prepared to investigate the effect of Zn^{2+} concentration in hydrothermal solution on the morphology and performance of the composited sorbents. As shown in Figure. S5a, manganese oxides were found to be randomly scattered on supporters with bulk crystals in large particle size when Zn^{2+} was not introduced in the hydrothermal process. While for that of the sorbent Zn@MnO_x /24PCNFs, it was suggested that the addition of Zn^{2+} could inhibit the formation of bulk crystals, thus forming uniformly dispersed particles on 24PCNFs (Figure. S5b). As far as the concentration of Zn^{2+} reached up to 0.02 M, in addition to nano particles anchored on the carbon nanofibers, nanowires with length of 50-80 nm appeared within the nanofibers have been observed in the sorbent Zn2@MnO_x /24PCNFs (Figure. S5c). Besides, the quantity of nanowire increased when the content of Zn went up to 0.03 M (Figure. S5d). By analyzing the elemental mapping graphs of sorbents ZnY@MnO_x /24PCNFs in Figure. S5, the nanoparticles anchored on porous carbon nanofibers could be attributed to zinc oxide and manganese oxides, while the nanowires between the fibers may be the excessive zinc oxide that restricted by the attachment sites on CNFs. The presence of nanowires can improve the sulfur capacity of the composite sorbents only through the way of increasing the content of active components (Table S1), but its utilization rate is low according to their large size and the uneven distribution. Therefore, based on the above analyses, sorbent Zn@MnO_x /24PCNFs was selected as the optimal composited sorbents, in which the active components were uniformly anchored on porous carbon nanofibers, and the active components that in the shape of nanowires and bulk crystals were absent.

Figure. 2d shows the TEM image of PCNFs, the structure of nanofibers embedded with hollow carbon shells can be clearly observed. The structures of MnO_x /24PCNFs (Figure. 2e) and Zn@MnO_x /24PCNFs (Figure. 2f) were similar to the original PCNFs, verifying that the results from SEM. Figures. 2g-i represent the corresponding enlarged TEM images of Figures. 2d-f, respectively, showing that the carbon layer thickness of the hollow carbon shells was about 12 nm. Compared with 24PCNFs, the surface of MnO_x /24PCNFs after oxidation treatment was darker in many regions (Figure. 2h), which could be the anchored ‘seed layer’ of manganese oxides, as verified by elemental mapping images of MnO_x /24PCNFs (Figure. S6). Evenly distributed granular active components with diameter around 3.1-13.0 nm have been observed in sorbent Zn@MnO_x /24PCNFs. The EDX elemental mapping images in Figure. 2j also prove the even distributions of elements O, Zn and Mn.

Structural performance of various CNFs-derived supporters and loaded sorbents has been investigated to reveal the variations under different compositions of the spinning solution as well as the changes before and after oxidation and hydrothermal processes. As shown in Figure. S7 and Table S2, the smooth surface and absence of pores led to low specific surface area ($51.765 \text{ m}^2 \text{ g}^{-1}$) of CNFs, which is not conducive to gas

adsorption. Therefore, PVP was added in the spinning solution to modify the structural parameters due to its low carbon yield after decomposition that increasing the micro-pores.²¹⁻²³ As a result, 0PCNFs exhibited specific surface area of 275.077 m²g⁻¹ and pore volume of 0.169 cm³g⁻¹.

Further, SiO₂ was also introduced to increase the pore volume. After the introduction of SiO₂, the specific surface area of 8PCNFs was 145.193 m² g⁻¹, the reduction from 0PCNFs was due to the fact that part of micro-pores was destroyed and only a small count of hollow carbon shells was generated in 8PCNFs. With the increase of SiO₂, the specific surface area of 16PCNFs, 24PCNFs and 32PCNFs was similar to that of 0PCNFs and pore volume values increased largely, which were 0.200, 0.228 and 0.247 cm³g⁻¹, respectively (**Figure. 3a**). The adsorption-desorption isotherm curves of 16PCNFs, 24PCNFs and 32PCNFs all showed type IV isotherms with a weak H4-type hysteresis loop ($P/P_0^{-1} > 0.5$) according to the IUPAC classification, suggesting the presence of slit shaped mesopores.^{24,25} These results indicate that with the increase of the content of hollow carbon shells embedded on porous carbon nanofibers, the structure of pristine CNFs was completely changed and exhibited positive effect of SiO₂ on the enlargement of surface area and pore volume.

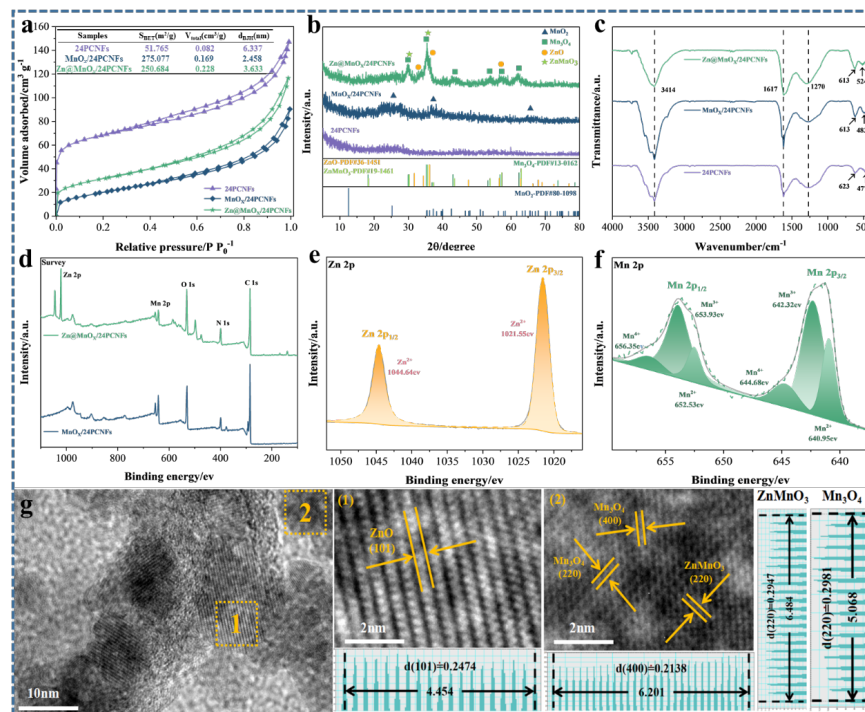


Figure 3 . (a) N₂ adsorption-desorption curves and structural parameters, (b) XRD patterns and (c) FT-IR spectra of 24PCNFs, MnO_x/24PCNFs and Zn@MnO_x/24PCNFs. (d) XPS spectra of MnO_x/24PCNFs and Zn@MnO_x/PCNFs. Fitted XPS spectra of elements (e) Zn, (f) Mn, (g) high resolution TEM graphs and lattice fringe analyses of sorbent Zn@MnO_x/24PCNFs.

After activation, the specific surface area and pore volume of sorbents MnO_x/CNFs and MnO_x/XCNFs decreased sharply and displayed a unified trend with the increased content of SiO₂. Taking MnO_x/24PCNFs as a sample, whose specific surface area and pore volume decreased of from 250.684 m²g⁻¹ and 0.228 cm³g⁻¹ of 24PCNFs to 70.280 m²g⁻¹ and 0.140 cm³g⁻¹ of MnO_x/24PCNFs, respectively, which may be due to the blocking of micro-pores by the anchored manganese oxides (Figures. 3a and S8, Table S2).²⁶ Interestingly, an increase in the pore size of MnO_x/XCNFs sorbents have been observed, which is beneficial to alleviate the reduction of specific surface area after oxide loading to improve the gas adsorption performance. During the hydrothermal process, the attachment of zinc oxide generates new micro structures on the original

basis, which is the reason why the specific surface area and pore volume ($113.854 \text{ m}^2\text{g}^{-1}$ and $0.180 \text{ cm}^3\text{g}^{-1}$) of $\text{Zn@MnO}_x/24\text{PCNFs}$ are better than $\text{MnO}_x/24\text{PCNFs}$. BET characterizations were also performed on $\text{ZnY@MnO}_x/24\text{PCNFs}$ sorbents to reveal the effect of loading content of ZnO on pore structures of sorbents. As shown in Figure. S9 and Table S2, the pore volume values of $\text{ZnY@MnO}_x/24\text{PCNFs}$ sorbents with different Zn^{2+} content were similar but the specific surface area decreased slightly with the increase of Zn^{2+} contents in hydrothermal solution, which might be caused by the aggregation of excessive ZnO particles and the increase of ZnO nanowires.

Figure. 3b shows the XRD patterns of 24PCNFs, $\text{MnO}_x/24\text{PCNFs}$ and $\text{Zn@MnO}_x/24\text{PCNFs}$. 24PCNFs possessed a relatively broad diffraction peak at around 2θ for the presence of C, which corresponded to the (002) planes of graphite carbon.^{27,28} Besides, no added diffraction peaks of XPCNFs were observed to that of CNFs, indicating that no impurities were introduced in the etching process (Figure. S10). The broad diffraction peaks appeared at 25.2° , 37.3° and 65.6° of sorbent $\text{MnO}_x/24\text{PCNFs}$ could be attributed to the (002), (-111) and (020) planes of MnO_2 .²⁹ Characteristic peaks in the same location but with different intensities were found in the XRD patterns of sorbents MnO_x/CNFs and $\text{MnO}_x/\text{XPCNFs}$, implying that nanosized MnO_2 was successfully loaded on carbon nanofibers with different structures but there were more manganese oxides loaded on sorbent with XPCNFs as supporter, which was influenced by their bigger surface area (Figure. S11). After hydrothermal growth of ZnO, weak diffraction peaks at $2\theta = 34.4^\circ$, 36.2° and 56.6° were assigned to the (002), (101) and (110) planes of the ZnO (No. JCPDS 36-1451).³⁰ Besides, the strong diffraction peaks at $2\theta = 30.2^\circ$ and 35.6° were assigned to the (220), and (311) planes of the ZnMnO_3 (No. JCPDS 19-1461).³¹ The above phenomenon indicated that the particles anchored on 24PCNFs were the composited oxides of Zn and Mn, in which the part of Zn^{2+} was directly loaded on manganese oxide as ZnO, while the other part was combined with manganese oxide to form ZnMnO_3 within sorbent $\text{Zn@MnO}_x/24\text{PCNFs}$. In addition, the trace of Mn_3O_4 (No. JCPDS 13-0162) was also found after hydrothermal according to the strong diffraction peaks at $2\theta = 29.9^\circ$, 35.3° , 12.7° , 43.0° , 53.2° , 56.7° and 62.3° , which could be assigned to the (220), (311), (400), (422), (511) and (440) planes of Mn_3O_4 .³² The XRD patterns of $\text{Zn0@MnO}_x/24\text{PCNFs}$, $\text{Zn2@MnO}_x/24\text{PCNFs}$ and $\text{Zn3@MnO}_x/24\text{PCNFs}$ were also showed in Figure. S12. It was found that MnO_2 was easily reduced to Mn_3O_4 (No. JCPDS 80-0382) with better crystalline when there was no Zn^{2+} in the hydrothermal solution, which was verified by the sharp peaks of at $2\theta = 18.0^\circ$, 28.9° , 30.9° , 32.3° , 36.0° , 44.4° , 50.8° and 58.4° within sorbent $\text{Zn0@MnO}_x/24\text{PCNFs}$.³³ While in contrast to sorbent $\text{Zn@MnO}_x/24\text{PCNFs}$, strong and sharp diffraction peaks of ZnO appeared upon sorbent $\text{Zn2@MnO}_x/24\text{PCNFs}$. With the further increase of Zn^{2+} concentration in hydrothermal solution, the diffraction peaks of ZnO in sorbent $\text{Zn3@MnO}_x/24\text{PCNFs}$ were much stronger, indicating the existence of ZnO nanowires with complete crystalline between carbon nanofibers, which was basically consistent with the results from SEM and elemental mapping images.

The FT-IR spectra of 24PCNFs, $\text{MnO}_x/24\text{PCNFs}$ and $\text{Zn@MnO}_x/24\text{PCNFs}$ are exhibited in Figure. 3c. Characteristic peaks at 3414 , 1617 and 1278 cm^{-1} were similar in all the three samples, relating to the stretching vibrations of -OH, C=O and C-C, respectively.³⁴ The carboxylic groups in the samples were mainly originated from the etching treatment. Si containing peaks were observed at 623 and 477 cm^{-1} of 24PCNFs that belong to the stretching vibration of Si-O and O-Si-O from silicate, suggesting the completely removing of SiO_2 .³⁵ After oxidation and hydrothermal processes, peaks that corresponding to Mn-O (613 , 483 cm^{-1}) and Zn-O (524 cm^{-1}) were recorded, implying that the sorbents $\text{MnO}_x/24\text{PCNFs}$ and $\text{Zn@MnO}_x/24\text{PCNFs}$ have been successfully synthesized.^{36,37}

The chemical composition and state of elements in sorbents $\text{MnO}_x/24\text{PCNFs}$ and $\text{Zn@MnO}_x/24\text{PCNFs}$ composites were examined by XPS, as shown in Figure. 3d, in which elements C, N, O and Mn were identified, while element Zn was traced in spectrum of $\text{Zn@MnO}_x/24\text{PCNFs}$. High resolution spectrum of Mn 2p was presented to investigate the properties of Mn in the as-prepared sorbent $\text{MnO}_x/24\text{PCNFs}$. As seen from Figure. S13a, the Mn $2p_{3/2}$ peak and Mn $2p_{1/2}$ peak could be decomposed to three parts, namely, Mn^{2+} (641.40 eV), Mn^{4+} (642.13 eV) and Mn^{3+} (644.92 eV), respectively.³⁸ C 1s spectrum in Figure. S13b could be deconvoluted into three peaks, C-C (284.66 eV), C=N (285.42 eV) and O-C=O (288.14 eV), and the presents of O-C=O bonds representing the partial oxidation of the surface carbon layer.³⁹ While the spectrum of N 1s could be fitted into four peaks, which corresponding to pyridinic N (398.28 eV), pyrrolic N (400.10

eV), graphitic N (402.25 eV) and oxidized N (406.60 eV), respectively (Figure. S13c).^{40,41} Deconvoluted peaks of the O 1s spectrum were centered at 529.58, 531.11, 532.59 and 533.97 eV, respectively (Figure. S13d). The lower binding energy located at 529.58 and 531.11 eV could be attributed to the O²⁻ forming oxide with manganese (Mn-O-Mn, Mn-O-C) and the hydroxide (Mn-O-H), respectively.^{42,43} While the latter two peaks were assigned to O-C=O and H₂O.⁴⁴ The high resolution XPS spectra of the C 1s, N 1s, O 1s, Mn 2p and Zn 2p of Zn@MnO_x/24PCNFs were presented in Figures. 3e and f, S18e-g. The Mn 2p_{3/2} peak were consisted of three separated peaks at 640.95, 642.32 and 644.68 eV, which were in accordance with Mn²⁺, Mn³⁺ and Mn⁴⁺, respectively.⁴⁵ It could be inferred that element manganese was mainly in the state of Mn²⁺ and Mn³⁺, and the relative content ratio of Mn²⁺/Mn³⁺ was close to 1:2, indicating that manganese oxide was partially in the form of Mn₃O₄. Figure. 3f displays two sharp peaks of Zn 2p_{3/2} and Zn 2p_{1/2} at binding energy of 1021.55 and 1044.64 eV, implying the oxidation status of ZnO and ZnMnO₃ in Zn@MnO_x/24PCNFs.^{46,47} The C 1s and N 1s spectra of sorbent Zn@MnO_x/24PCNFs were almost the same as that in the sorbent MnO_x/24PCNFs, which were both deconvoluted into three peaks, respectively (Figure. S13e and f). Deconvoluted peaks of O 1s spectrum were resolved into, 529.76, 530.89, 531.58, 532.47 and 533.57 eV, attributing to Mn-O-Mn (or Mn-O-C), Zn-O, Mn-O-H, O-C=O and H₂O, respectively (Figure. S13g).⁴⁷ Based on the above analyses, both the ‘seed layer’ of MnO_x and Zn@MnO_x nanoparticles were successfully anchored at 24PCNFs through strong chemical bonds.

High-resolution TEM images of sorbent Zn@MnO_x/24PCNFs in Figure. 3g indicated the presence of ZnO, Mn₃O₄ and ZnMnO₃. Specifically, the lattice fringes with spacing distances of 0.2474, 0.2138, 0.2981 and 0.2947 nm could be recognized, corresponding to the planes of (101) in ZnO, (400) and (220) in Mn₃O₄, and (220) in ZnMnO₃, respectively. The above results are consistent with those observed by XRD and XPS. Besides, the HRTEM image of MnO_x/24PCNFs was displayed in Figure. S14, no obvious lattice fringes were found, indicating that manganese oxides were existed in grains with small size and high dispersion.

Furthermore, the as-prepared MnO_x/24PCNFs and Zn@MnO_x/24PCNFs sorbents were applied to remove H₂S at 500 °C for practical application. In **Figures. 4a**, S15 and S16, it was found that the active component MnO_x and Zn@MnO_x transferred to the products of MnS (No. JCPDS 88-2223) and (Zn, Mn)S (No. JCPDS 11-0513) after the desulfurization reaction, respectively. The representative peaks at 34.3° and 49.3° corresponded to the (200) and (220) planes of MnS, besides, the strong diffraction peaks at 26.5°, 28.2°, 30.1°, 46.8°, 51.1° and 55.6° were assigned to the (100), (002), (101), (110), (103) and (112) planes of the (Zn, Mn)S.⁴⁸ However, XRD diffraction peaks of ZnY@MnO_x/24PCNFs sorbents with different contents of active components were different after desulfurization (Figure. S16). It can be seen that the used Zn0@MnO_x/24PCNFs sorbent exhibited diffraction peaks of MnS and MnO (No. JCPDS 78-0424), suggesting that Mn₃O₄ was transformed in the presence of H₂S to MnS and MnO with poor utilization rate of Mn²⁺. XRD patterns of Zn2@MnO_x/24PCNFs and Zn3@MnO_x/24PCNFs after desulfurization showed that they were mainly consisted of (Zn, Mn)S and ZnO crystals. The strong ZnO diffraction peaks came from ZnO nanowires that were not fully involved in the desulfurization reaction. In conclusion, this is the reason for the much higher utilization rate of active components of sorbent Zn@MnO_x/24PCNFs than that of the sorbents contained ZnO nanowires.

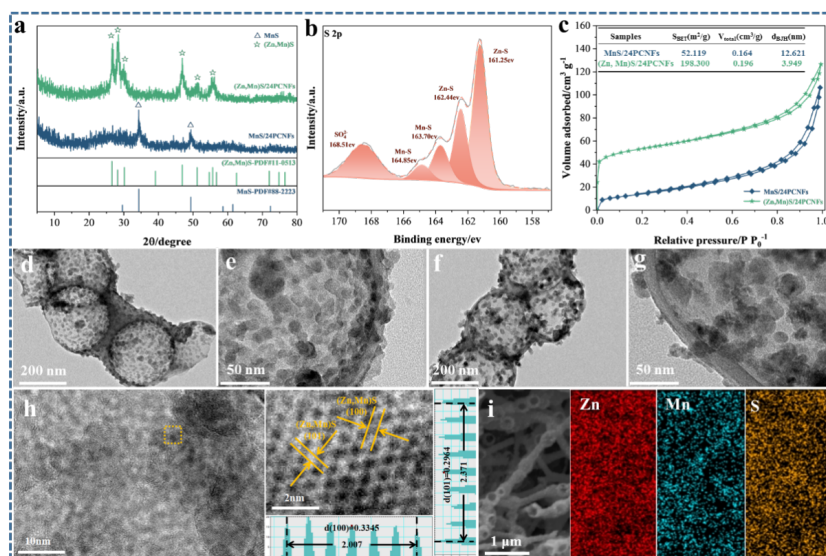


Figure 4 . (a) XRD patterns of MnS/24PCNFs and (Zn, Mn)S/24PCNFs. (b) Fitted XPS spectra S 2p in (Zn, Mn)S/24PCNFs. (c) N₂ adsorption-desorption curves and structural parameters, TEM graphs of (d, e) MnS/24PCNFs and (f, g) (Zn, Mn)S/24PCNFs. (h) high resolution TEM graphs and lattice fringe analyses, (i) elemental mapping graphs of elements Zn, Mn and S of (Zn, Mn)S/24PCNFs.

Chemical compositions and states of elements in the desulfurized sorbents MnS/24PCNFs and (Zn, Mn)S/24PCNFs were characterized using XPS technology. As shown in Figure. S17a, the desulfurization process introduced element S into sorbents MnO_x/24PCNFs and Zn@MnO_x/24PCNFs. High-resolution XPS spectra of the S 2p in MnS/24PCNFs showed characteristic peaks at 161.90 and 163.11 eV, which could be derived from the bond of S-Mn-S, while the peaks at 163.73 and 164.91 eV were attributed to the bond Mn-S, implying that the main sulfide products were manganese sulfides (Figure. S18b).⁴⁹⁻⁵¹ While for the XPS spectra of S 2p in sorbent (Zn, Mn)S/24PCNFs, the peaks at 161.25, 162.44 eV and 163.70, 164.85 eV should be attributed to the bonds of Zn-S and Mn-S, respectively.⁵² Besides, the proportion of bond Zn-S was much higher than that belonged to MnS when referring to the multiples fitting of the S 2p peaks (Figure. 4b). In addition, the characteristic peaks belonged to SO₄²⁻ may be the result of the adsorption of water by SO₂ generated from the oxidation of H₂S.⁵³ Moreover, by comparing the O 1s spectra of MnO_x/24PCNFs and Zn@MnO_x/24PCNFs before and after desulfurization, it was found that the relative content of Mn-O decreased, and the fitting peak of Zn-O disappeared in the O 1s spectra of (Zn, Mn)S/24PCNFs. These also indicate that desulfurization reaction is a replacement process between O²⁻ and S²⁻ (Figure. S17c-d).

Structural performance of desulfurized MnS/24PCNFs and (Zn, Mn)S/24PCNFs has been investigated and represented in Figure. 4c and Table S2. The pore volume and pore size increased from 0.140 cm³ g⁻¹, 7.957 nm of MnO_x/24PCNFs to 0.164 cm³ g⁻¹, 12.621 nm of MnS/24PCNFs, respectively, while the specific surface area decreased from 70.280 m² g⁻¹ of MnO_x/24PCNFs to 52.119 m² g⁻¹ of MnS/24PCNFs. By combining the TEM graphs of sorbent MnO_x/24PCNFs displayed in Figure. 4d and e, it could be seen that the nanosized particles MnO_x transferred into MnS particles with diameter about 8-12 nm, meaning that the pore structure of MnO_x/24PCNFs before and after desulfurization changed obviously. The larger particle volume of the desulfurized products generated new structures with larger pore size and reduced the proportion of micro-pores that contributed a lot to the specific surface area. In the contrast, opposite trend in structural parameters of sorbents Zn@MnO_x/24PCNFs and (Zn, Mn)S/24PCNFs has been observed. Specifically, the specific surface area and pore volume increased of from 113.854 m² g⁻¹, 0.180 cm³ g⁻¹ of Zn@MnO_x/24PCNFs to 198.300 m² g⁻¹, 0.196 cm³ g⁻¹ of (Zn, Mn)S/24PCNFs, respectively (Table S2). The N₂ adsorption-desorption isotherm type (IV) and hysteresis ring type (H4) of sorbent (Zn, Mn)S/24PCNFs

were similar to that of Zn@MnO_x /24PCNFs, except for the sharp increasing in the region 0 <P P₀⁻¹< 0.1, representing the existence of massive micro-pores instead of macro- or meso-pores (Figure. 4c). The structural variations between sorbents before and after desulfurization were mainly attributed to the fact that O²⁻ in manganese oxide was replaced by S²⁻ in H₂S during desulfurization, which increased the size of active components and thus blocked meso-pores into micro-pores, and this is why the specific surface area increased and pore size decreased from 6.336 to 3.949 nm in the meantime.⁵⁴ TEM analysis was also performed to observe the morphology changes of (Zn, Mn)S/24PCNFs. The particle size of desulfurization products was found to be in range of 9.1-23.0 nm, which was increased as compared to that of fresh sorbent due to the fact that the MnS and ZnS are much larger than MnO_x and ZnO in molecular size (Figure. 4f and g). High-resolution TEM images of (Zn, Mn)S/24PCNFs in Figure. 4h implied the presence of zinc sulfide and manganese sulfide according to the lattice fringes with spacing distances of 0.3345 and 0.2964 nm, respectively. In addition, elemental mapping graphs in Figure. 4i indicated the even distribution of the elements Zn and Mn after desulfurization, meaning the high stability of the as-prepared sorbent.

Furthermore, deconvoluted peaks of Mn 2p_{3/2} spectrum of MnS/24PCNFs were resolved into three parts, namely 640.73 and 642.03 eV, attributing to Mn²⁺ of MnS and MnO, respectively, while the peak located at 645.32 eV could be attributed to Mn⁴⁺ (Figure. S17e). However, the Mn 2p_{3/2} peak of used (Zn, Mn)S/24PCNFs was consisted of four separated peaks (Figure. S17f), the difference from MnS/24PCNFs was that the peak represented Mn⁴⁺ at 641.10 eV and the peak located at binding energies of 644.87 corresponded to the shake-up satellite. Moreover, as shown in Figure. S18g, the two peaks at binding energies of 1021.51 and 1044.56 eV were consistent with Zn2p_{3/2} and Zn2p_{1/2}, respectively, indicating the oxidation state of Zn was Zn²⁺.⁵⁵

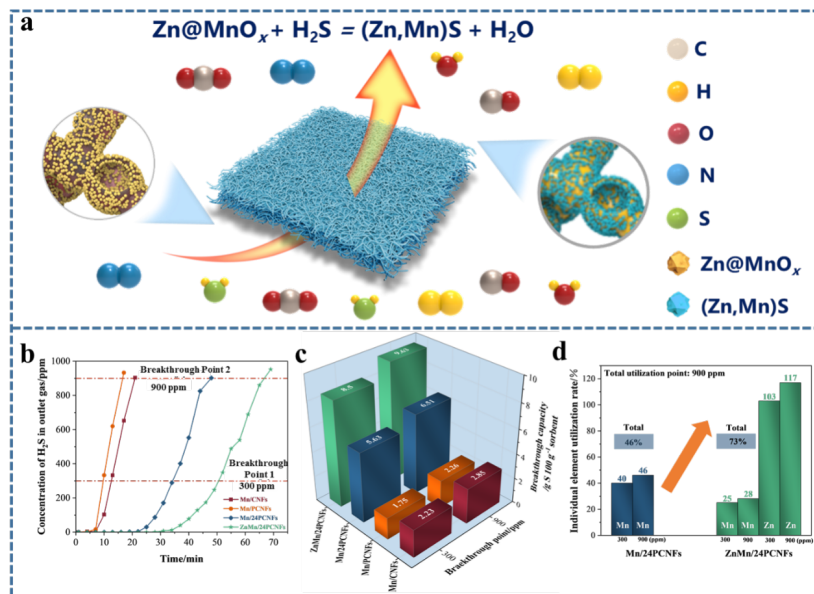
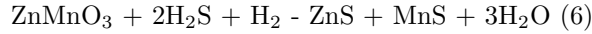
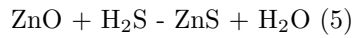
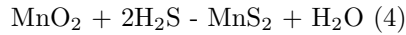


Figure 5 . (a) Illustration of desulfurization process of sorbent Zn@MnO_x /PCNFs. (b) Breakthrough curves, (c) sulfur capacities of sorbents MnO_x /CNFs, MnO_x /0PCNFs, MnO_x /24PCNFs and Zn@MnO_x /24PCNFs. (d) Utilization rates of active components of sorbents MnO_x /24PCNFs and Zn@MnO_x /24PCNFs.

Based on the above analyses, the process of H₂S removal upon sorbents MnO_x /24PCNFs and Zn@MnO_x /24PCNFs was proposed as the reactions and illustration graph displayed (**Figure. 5a**) .





The desulfurization performance of MnO_x/CNFs , $\text{MnO}_x/\text{XPCNFs}$ and $\text{ZnY@MnO}_x/24\text{PCNFs}$ sorbents was also tested to uncover the influential factors behind the sorbent performance (Figure. 5b). Figure. S18a and b showed the breakthrough curves and the total sulfur capacities at the detection point of 900 ppm. The breakthrough sulfur capacities of various sorbents were ranked in the following order: $\text{Zn3@MnO}_x/24\text{PCNF} > \text{Zn2@MnO}_x/24\text{PCNF} > \text{Zn@MnO}_x/24\text{PCNF} > \text{MnO}_x/32\text{PCNFs} > \text{MnO}_x/24\text{PCNFs} > \text{MnO}_x/16\text{PCNFs} > \text{Zn0@MnO}_x/24\text{PCNFs} > \text{MnO}_x/8\text{PCNFs} > \text{MnO}_x/\text{CNFs} > \text{MnO}_x/0\text{PCNFs}$, which was consistent with the content order of active components in different sorbents. As shown in Figure. 5b and c, the breakthrough sulfur capacity of $\text{MnO}_x/24\text{PCNFs}$ sorbent ($6.51 \text{ g S } 100 \text{ g}^{-1} \text{ sorbent}$) was 2.3 and 2.8 times higher than that of the sorbents MnO_x/CNFs and $\text{MnO}_x/0\text{PCNFs}$, respectively, which was also in the same trend with the content of Mn^{2+} loaded on the corresponding sorbents. This phenomenon is mainly attributed to the different structure types of the sorbents, of which the effect of massive micro-pores within supporter 0PCNFs exceeded that of its high specific surface area. In contrast, the meso- and macro-pores within supporter 24PCNFs contributed greatly to the improvements in loading content and desulfurization performance of the sorbent $\text{MnO}_x/24\text{PCNFs}$.

After the ZnO nanoparticles anchored on $\text{MnO}_x/24\text{PCNFs}$ via hydrothermal reaction, the sulfur capacity of sorbents $\text{ZnY@MnO}_x/24\text{PCNFs}$ all increased. Although the sulfur capacity of $\text{Zn2@MnO}_x/24\text{PCNFs}$ and $\text{Zn3@MnO}_x/24\text{PCNFs}$ was higher than that of $\text{Zn@MnO}_x/24\text{PCNFs}$ ($9.63 \text{ g S } 100 \text{ g}^{-1} \text{ sorbent}$), but their utilization rates of active components were far behind due to ZnO nanowires were not fully participated in desulfurization. More important, the total utilization of active components increased from 46% of $\text{MnO}_x/24\text{PCNFs}$ to 73% of $\text{Zn@MnO}_x/24\text{PCNFs}$ (Figure. 5d). These results indicate that the introduction of ZnO not only increased the sulfur capacity, but also improves the total utilization of active components. Among them, the utilization of ZnO was up to 117%, owing the uniform dispersion of ZnO on the surface of $\text{MnO}_x/24\text{PCNFs}$.

3. Conclusions

In conclusion, the combination of electrospinning, etching, oxidation activation and hydrothermal treatments has been applied to synthesize the surface area enlarged CNFs supported Zn-Mn-based sorbents for high temperature coal gas desulfurization. SiO_2 was introduced as hard template for the purpose of creating hollow carbon shells on CNFs, then enlarging the surface area of the porous carbon nanofibers and increasing the loading content of active components. As revealed in the various characterizations, the modified PCNFs that with 24 wt.% SiO_2 possess a specific surface area of $250.684 \text{ m}^2 \text{ g}^{-1}$ and a Mn^{2+} loading content of 17.8 wt.%, which are 4.9 and 3.3 times higher than that of pristine CNFs. More important, the sulfur capacity of sorbent supported by 24PCNFs is 2.3 times higher than that with pristine CNFs. Furthermore, the existence of MnO_x ‘seed layer’ also serves for the uniformly growth of nanosized ZnO and the promotion of desulfurization performance of the as-prepared sorbent. $\text{Zn@MnO}_x/24\text{PCNFs}$ sorbent prepared with 24 wt.% SiO_2 and 0.01 M Zn^{2+} possesses an optimal breakthrough capacity ($9.63 \text{ g S } 100 \text{ g}^{-1} \text{ sorbent}$) and excellent utilization rate of active components (overall 73%) with a high utilization rate of ZnO reaches up to 117%. Methods like TEM and SEM suggest that the contributions come from the synergetic effects of the enlarged surface area of porous carbon nanofibers and the oxidation of KMnO_4 that providing the potentials for rapid mass transfer and chemical reaction. In brief, the PCNFs supported Zn-Mn bimetallic desulfurization sorbent can facilitate the H_2S clean-up in electric power plant and coal chemical industry.

Acknowledgement

This work was funded by the National Natural Science Foundation of China (No. 21908156, 21978188, 52202256, and 22075046), Natural Science Funds for Distinguished Young Scholar of Fujian Province (2020J06038), Natural Science Foundation of Jiangsu Province of China (BK20220612), and China Postdoctoral Science Foundation (2021T140431). We also acknowledge the funds from the project of Jiangsu University “Qinglan Project”.

Conflict of interest

The authors declare no conflict of interest.

References

1. Guo X, Wang X, Zheng D, Feng D. Effect of coal consumption on the upgrading of industrial structure. *Geofluids*. 2022;2022:4313175.
2. Liang S, Peng B, Liu S, et al. Low-temperature highly efficient and selective removal of H₂S over three-dimensional Zn-Cu-based materials in an anaerobic environment. *Environ Sci Technol*. 2020;54(10):5964-5972.
3. Liu Q, Liu B, Liu Q, Guo S, Wu X. Probing mesoporous character, desulfurization capability and kinetic mechanism of synergistic stabilizing sorbent Ca_xCu_yMn_zO_i/MAS-9 in hot coal gas. *J Colloid Interface Sci*. 2021;587:743-754.
4. Feng Y, Lu J, Wang J, et al. Desulfurization sorbents for green and clean coal utilization and downstream toxics reduction: A review and perspectives. *J Clean Prod*. 2020;273:123080.
5. Yang H, Tatarchuk B. Novel-doped zinc oxide sorbents for low temperature regenerable desulfurization applications. *AIChE J*. 2010;56(11):2898-2904.
6. Sun Y, Zhang X, Zhang M, et al. Rational design of electrospun nanofibers for gas purification: Principles, opportunities, and challenges. *Chem Eng J*. 2022;446:137099.
7. Canning G, Azzam S, Hoffman A, et al. Lanthanum induced lattice strain improves hydrogen sulfide capacities of copper oxide adsorbents. *AIChE J*. 2021;67(12):e17484.
8. Feng Y, Wen J, Hu Y, Wu B, Wu M, Mi J. Evaluation of the cycling performance of a sorbent for H₂S removal and simulation of desulfurization-regeneration processes. *Chem Eng J*. 2017;326:1255-1265.
9. Luo J, Wang C, Liu J, et al. High-performance adsorptive desulfurization by ternary hybrid boron carbon nitride aerogel. *AIChE J*. 2021;67(9):e17280.
10. Liu Q, Zhang Z, Liu B, Xia H. Rare earth oxide doping and synthesis of spinel ZnMn₂O₄/KIT-1 with double gyroidal mesopores for desulfurization nature of hot coal gas. *Appl Catal B-Environ*. 2018;237:855-865.
11. Wu M, Li Q, Wang X, Mi J. Structure characteristics and hot-coal-gas desulfurization properties of Zn-based sorbents supported on mesoporous silica with different pore-arrangement patterns: A comparison study. *Energ Fuel*. 2021;35(3):2456-2467.
12. Thompson J. Acid gas adsorption on zeolite SSZ-13: Equilibrium and dynamic behavior for natural gas applications. *AIChE J*. 2020;66(10):e16549.
13. Zhang X, Xiong W, Peng L, Wu Y, Hu X. Highly selective absorption separation of H₂S and CO₂ from CH₄ by novel azole-based protic ionic liquids. *AIChE J*. 2020;66(6):e16936.
14. Feng Y, Wang J, Hu Y, Lu J, Zhang M, Mi J. Microwave heating motivated performance promotion and kinetic study of iron oxide sorbent for coal gas desulfurization. *Fuel*. 2020;267:117215.
15. Armstrong M, Shi X, Shan B, Lackner K, Mu B. Rapid CO₂ capture from ambient air by sorbent-containing porous electrospun fibers made with the solvothermal polymer additive removal technique. *AIChE*

J. 2019;65(1):214-220.

16. Liu R, Hou L, Yue G, et al. Progress of fabrication and applications of electrospun hierarchically porous nanofibers. *Adv Fiber Mater.* 2022;4(4):604-630.

17. Bajaj B, Joh HI, Jo SM, Park JH, Yi KB, Lee S. Enhanced reactive H₂S adsorption using carbon nanofibers supported with Cu/Cu_xO nanoparticles. *Appl Surf Sci.* 2018;429:253-257.

18. Kim S, Bajaj B, Byun CK, et al. Preparation of flexible zinc oxide/carbon nanofiber webs for mid-temperature desulfurization. *Appl Surf Sci.* 2014;320:218-224.

19. Jun J, Lee JS, Shin DH, Kim SG, Jang J. Multidimensional MnO₂ nanohair-decorated hybrid multichannel carbon nanofiber as an electrode material for high-performance supercapacitors. *Nanoscale.* 2015;7(38):16026-16033.

20. Wang L, Li X, Li Q, et al. Oriented polarization tuning broadband absorption from flexible hierarchical ZnO arrays vertically supported on carbon cloth. *Small.* 2019;15(18):1900900.

21. de Oliveira JB, Guerrini LM, Oishi SS, et al. Carbon nanofibers obtained from electrospinning process. *Mater Res Express.* 2018;5(2):025602.

22. Qiu Y, Li G, Hou Y, et al. Vertically aligned carbon nanotubes on carbon nanofibers: a hierarchical three-dimensional carbon nanostructure for high-energy flexible supercapacitors. *Chem Mater.* 2015;27(4):1194-1200.

23. Hu J, Li C, Li L, et al. Phytic acid assisted preparation of high-performance supercapacitor electrodes from noncarbonizable polyvinylpyrrolidone. *J Power Sources.* 2020;448:227402.

24. Karthikeyan KK, Biji P. A novel biphasic approach for direct fabrication of highly porous, flexible conducting carbon nanofiber mats from polyacrylonitrile (PAN)/NaHCO₃ nanocomposite. *Micropor Mesopor Mater.* 2016;224:372-383.

25. Zhao Y, Lai Q, Wang Y, Zhu J, Liang Y. Interconnected hierarchically porous Fe, N-codoped carbon nanofibers as efficient oxygen reduction catalysts for Zn-air batteries. *ACS Appl Mater Interfaces.* 2017;9(19):16178-16186.

26. Kang S, Park Dh, Hwang J. Hierarchical ZnO nano-spines grown on a carbon fiber seed layer for efficient VOC removal and airborne virus and bacteria inactivation. *J Hazard Mater.* 2022;424:127262.

27. Zhang P, Shao C, Zhang Z, et al. In situ assembly of well-dispersed Ag nanoparticles (AgNPs) on electrospun carbon nanofibers (CNFs) for catalytic reduction of 4-nitrophenol. *Nanoscale.* 2011;3(8):3357-3363.

28. Zhang Z, Li X, Wang C, Fu S, Liu Y, Shao C. Polyacrylonitrile and carbon nanofibers with controllable nanoporous structures by electrospinning. *Macromol Mater Eng.* 2009;294(10):673-678.

29. Zhao P, Yao M, Ren H, Wang N, Komarneni S. Nanocomposites of hierarchical ultrathin MnO₂ nanosheets/hollow carbon nanofibers for high-performance asymmetric supercapacitors. *Appl Surf Sci.* 2019;463:931-938.

30. Luo D, Fei J, Zhang C, Li H, Zhang L, Huang J. Optimization of mechanical and tribological properties of carbon fabric/resin composites via controlling ZnO nanorods morphology. *Ceram Int.* 2018;44(13):15393-15401.

31. Chen H, Ding L-X, Xiao K, Dai S, Wang S, Wang H. Highly ordered ZnMnO₃ nanotube arrays from a “self-sacrificial” ZnO template as high-performance electrodes for lithium ion batteries. *J Mater Chem A.* 2016;4(42):16318-16323.

32. Li N, Wang J-Y, Liu Z-Q, et al. One-dimensional ZnO/Mn₃O₄ core/shell nanorod and nanotube arrays with high supercapacitive performance for electrochemical energy storage. *RSC Adv.* 2014;4(33):17274-17281.
33. Ashoka S, Nagaraju G, Chandrappa GT. Reduction of KMnO₄ to Mn₃O₄ via hydrothermal process. *Mater Lett.* 2010;64(22):2538-2540.
34. Tucureanu V, Matei A, Avram AM. FT-IR spectroscopy for carbon family study. *Crit Rev Anal Chem.* Nov 2016;46(6):502-520.
35. Gaggiano R, De Graeve I, Mol JMC, Verbeken K, Kestens LAI, Terryn H. An infrared spectroscopic study of sodium silicate adsorption on porous anodic alumina. *Surf Interface Anal.* 2013;45(7):1098-1104.
36. Singh M, Kaur M, Sangha MK, Ubhi MK. Comparative evaluation of manganese oxide and its graphene oxide nanocomposite as polyphenol oxidase mimics. *Mater Today Commun.* 2021;27:102237.
37. Liu Z, Xing Y, Fang S, et al. Low temperature self-assembled synthesis of hexagonal plate-shape Mn₃O₄ 3D hierarchical architectures and their application in electrochemical capacitors. *RSC Adv.* 2015;5(68):54867-54872.
38. Chi HZ, Tian S, Hu X, Qin H, Xi J. Direct growth of MnO₂ on carbon fiber cloth for electrochemical capacitor. *J Alloy Compd.* 2014;587:354-360.
39. Yang B, Quan H, Gao J, Wang S, Wang N, Sun C. MnO nanoparticles with cationic defects encapsulated in nitrogen-doped porous carbon for high-performance aqueous zinc-ion batteries. *J Alloy Compd.* 2021;889:161680.
40. Li W, Gao X, Chen Z, et al. Electrochemically activated MnO cathodes for high performance aqueous zinc-ion battery. *Chem Eng J.* 2020;402:125509.
41. Ayiania M, Smith M, Hensley AJR, Scudiero L, McEwen J-S, Garcia-Perez M. Deconvoluting the XPS spectra for nitrogen-doped chars: An analysis from first principles. *Carbon.* 2020;162:528-544.
42. Zhang J, Chu R, Chen Y, Zeng Y, Zhang Y, Guo H. Porous carbon encapsulated Mn₃O₄ for stable lithium storage and its ex-situ XPS study. *Electrochim Acta.* 2019;319:518-526.
43. Zheng X, Lian Q, Zhou L, Jiang Y, Gao J. Urchin-like trimanganese tetraoxide particles with oxidase-like activity for glutathione detection. *Colloids Surf A.* 2020;606:125397.
44. Zhu S, Li L, Liu J, et al. Structural directed growth of ultrathin parallel birnessite on beta-MnO₂ for high-performance asymmetric supercapacitors. *ACS Nano.* 2018;12(2):1033-1042.
45. Biesinger MC, Payne BP, Grosvenor AP, Lau LWM, Gerson AR, Smart RSC. Resolving surface chemical states in XPS analysis of first row transition metals, oxides and hydroxides: Cr, Mn, Fe, Co and Ni. *Appl Surf Sci.* 2011;257(7):2717-2730.
46. Gallegos MV, Peluso MA, Thomas H, Damonte LC, Sambeth JE. Structural and optical properties of ZnO and manganese-doped ZnO. *J Alloy Compd.* 2016;689:416-424.
47. Amin MS, Alshareef FM, Alsaggaf WT, Zaki ZI. Employing manufactured Mn₃O₄-ZnO nanocomposite for ameliorated photocatalytic performance under visible light. *Opt Mater.* 2022;127:112286.
48. Wang J, Ju F, Han L, et al. Effect of activated carbon supports on removing H₂S from Coal-based gases using Mn-based sorbents. *Energ Fuel.* 2015;29(2):488-495.
49. Qi K, Wang Y-Q, Rengaraj S, Al Wahaibi B, Mohamed Jahangir AR. MnS spheres: Shape-controlled synthesis and its magnetic properties. *Mater Chem Phys.* 2017;193:177-181.
50. Mariyappan V, Murugan K, Chen S-M. Solvothermal synthesis of carbon incorporated MnS₂ Spheres; high sensing performance towards the detection of furazolidone in bio-fluids. *J Alloy Compd.*

2021;882:160744.

51. Pham DT, Vu TT, Kim S, et al. A versatile pyramidal hauerite anode in congeniality diglyme-based electrolytes for boosting performance of Li- and Na-ion Batteries. *Adv Energy Mater.* 2019;9(37):1900710.
52. González-Chan IJ, Oliva AI. Physicochemical analysis and characterization of chemical bath deposited ZnS films at near ambient temperature. *J Electrochem Soc.* 2016;163(8):421-427.
53. Long JW, Wallace JM, Peterson GW, Huynh K. Manganese oxide nanoarchitectures as broad-spectrum sorbents for toxic gases. *ACS Appl Mater Interfaces.* 2016;8(2):1184-1193.
54. Li Q, Wang X, Zhang R, Mi J, Wu M. Insights into the effects of metal-ion doping on the structure and hot-coal-gas desulfurization properties of Zn-based sorbents supported on SBA-15. *Fuel.* 2022;315:123198.
55. Anjum M, Kumar R, Barakat MA. Visible light driven photocatalytic degradation of organic pollutants in wastewater and real sludge using ZnO-ZnS/Ag₂O-Ag₂S nanocomposite. *J Taiwan Inst Chem E.* 2017;77:227-235.

Hosted file

Graphical Abstract(1).docx available at <https://authorea.com/users/499793/articles/587024-porous-carbon-nanofibers-supported-zn-mnox-sorbents-with-high-dispersion-and-loading-for-hot-coal-gas-desulfurization>